

CrossMark  
click for updatesCite this: *J. Mater. Chem. A*, 2016, 4, 18153

## Influence of the substrate on the bulk properties of hybrid lead halide perovskite films†

Esteban Climent-Pascual,<sup>a</sup> Bruno Clasen Hames,<sup>b</sup> Jorge S. Moreno-Ramírez,<sup>c</sup> Angel Luis Álvarez,<sup>c</sup> Emilio J. Juárez-Perez,<sup>d</sup> Elena Mas-Marza,<sup>b</sup> Ivan Mora-Seró,<sup>\*b</sup> Alicia de Andrés<sup>\*a</sup> and Carmen Coya<sup>\*c</sup>

In addition to the known effect of the substrate on the interfacial properties of perovskite films, here we show that the bulk properties of hybrid lead halide perovskite films depend on the type of substrate used for film growth. Despite the relative large film thickness, ~600 nm, the roughness and nature of the substrate layer (glass, FTO, TiO<sub>2</sub> and PEDOT:PSS) affect not just the degree of preferential orientation and crystal grain size but also the lattice parameters of CH<sub>3</sub>NH<sub>3</sub>PbI<sub>3</sub> films synthesized from the PbCl<sub>2</sub> precursor. The obtained changes in lattice parameters indicate that the Pb–Pb distance varies by around 0.7%. We suggest that the substrate roughness and chemical nature determine the concentration of defects mainly by varying the chlorine content and probably by the incorporation of oxygen and iodine vacancies during film nucleation and growth. These differences also have consequences in the observed light induced transformations. Upon laser illumination, the formation of additional defects, most probably related to oxygen, is revealed by 110 and 165 cm<sup>-1</sup> Raman peaks. With increasing laser power the chemical transformation into PbO<sub>x</sub> is clearly identified by the 140 and 275 cm<sup>-1</sup> Raman peaks. The irreversible photoluminescence enhancement observed at low power with illumination time, also dependent on the substrate nature, is proposed to be due to the localization of the electron–hole excitons created in the vicinity of the light generated defects. These results shed light on the performance of the perovskite layer and help to understand how bulk processes, where ion migration is a conspicuous example, are severely affected by interfacial properties such as those imposed by the substrate.

Received 7th October 2016  
Accepted 19th October 2016

DOI: 10.1039/c6ta08695k

www.rsc.org/MaterialsA

### 1. Introduction

The structure and physical properties of hybrid perovskite organometallic halides CH<sub>3</sub>NH<sub>3</sub>MX<sub>3</sub> (M = Pb or Sn, X = Cl, Br or I) were first reported by Weber in 1978.<sup>1,2</sup> The first attempt to use CH<sub>3</sub>NH<sub>3</sub>MX<sub>3</sub> (X = Br and I) as a semiconductor sensitizer in dye-sensitized liquid junction-type solar cells was in 2009, leading to a power conversion efficiency (PCE) of 3–4%.<sup>3</sup> Research on photovoltaic devices based on these materials, however, was triggered in 2012 by the reported 10–11% PCE of a solid-state perovskite solar cell based on CH<sub>3</sub>NH<sub>3</sub>PbI<sub>3</sub><sup>4,5</sup> (in short MAPbI<sub>3</sub>) with a 500 h confirmed stability. Few materials have generated

so much research effort in recent years, allowing solar cells based on them to reach a top PCE up to 22.1% (KRICT, South Korea).<sup>6</sup> Also, MAPbI<sub>3</sub> crystallizes easily from the solution phase, enabling cost-effective processing such as spin-coating and printing. This development has been boosted by the band gap tailoring ability through chemical substitution, superior charge-transfer properties and, especially, advances in controlling the morphology and composition of these materials.<sup>7–13</sup>

However, despite its outstanding performance, there is still much about their working principles that remains poorly understood, such as their photophysical properties and their relationship with structure and morphology. One clear example is the influence of contacts, which affect charge separation and the interfacial properties of perovskite devices, but there are many results that point to a deeper influence. For example, the hysteresis observed in the operating conditions is tightly related to ion migration, which is a bulk property, and is also strongly dependent on the choice of contacts. Different explanations have been provided in order to understand the hysteresis observed for Perovskite Solar Cells (PSCs).<sup>14</sup> The most accepted hypothesis attributes part of this hysteresis to bulk ion

<sup>a</sup>Instituto de Ciencia de Materiales de Madrid (ICMM), Consejo Superior de Investigaciones Científicas, Cantoblanco, Madrid 28049, Spain. E-mail: ada@icmm.csic.es

<sup>b</sup>Institute of Advanced Materials (INAM), Universitat Jaume I, 12006 Castelló, Spain

<sup>c</sup>Escuela Técnica Superior de Ingeniería de Telecomunicación (ETSIT), Universidad Rey Juan Carlos, 28933 Madrid, Spain

<sup>d</sup>Energy Materials and Surface Sciences Unit, Okinawa Institute of Science and Technology Graduate University (OIST), Okinawa 904-0495, Japan

† Electronic supplementary information (ESI) available. See DOI: 10.1039/c6ta08695k

migration along the perovskite layer,<sup>15–17</sup> although this hysteresis is also strongly affected by the kind of substrate employed.<sup>18</sup> In this work we have investigated to what extent the substrate is influencing not just interfacial properties but also the bulk properties of perovskite films by the use of different oxide and non-oxide substrates.

In the case of iodine perovskites, used for photovoltaic devices, it is worth highlighting the role of Pb precursors in the properties of the MAPbI<sub>3</sub> layer.<sup>19</sup> Specifically, in this work, MAPbI<sub>3</sub> layers have been prepared using PbCl<sub>2</sub> precursor (in short MAPbI<sub>3</sub>:Cl) with a reported Cl content lower than 0.2% wt.<sup>20,21</sup> MAPbI<sub>3</sub>:Cl has demonstrated improved properties over MAPbI<sub>3</sub>. While the bandgap is nearly identical to that of MAPbI<sub>3</sub>, in MAPbI<sub>3</sub>:Cl the carrier diffusion length is one order of magnitude larger than that of the MAPbI<sub>3</sub> (exceeding 1 μm) and exhibits improved charge carrier properties due to its higher crystallinity.<sup>7,22–24</sup> It has been shown that the perovskite film is intrinsically heterogeneous in crystal size, and that Cl plays an important role in improving the crystallization process.<sup>20</sup> However, the influence of the underlying layer on the stability, lattice parameters, orientation and the structure-properties relationship needs further understanding.

Halide perovskites exhibit a complex structural behavior with an unclear room temperature (RT) structure; several tetragonal space groups have been proposed: *I4cm*, *I4/mcm*, and *I4/m*.<sup>25–27</sup> Lattice dynamics calculations reveal a significant coupling between low-frequency vibrational modes associated with the inorganic (PbX<sub>3</sub>)<sub>n</sub> framework and those of the organic CH<sub>3</sub>NH<sub>3</sub><sup>+</sup> cation, which emphasizes the interplay between molecular orientation and the corner-sharing octahedral framework in the structural transformations.<sup>28,29</sup> These particularities together with the high sensitivity to ambient conditions and the instability under laser irradiation lead to a difficulty in the determination of the Raman modes, which are, in general, very useful tools to track structural, compositional or electronic changes in solids. The low frequency part of the Raman spectrum is still unclear and there is a great diversity in the phonon identification, as well as in the reported evolution of the Raman peaks in different atmospheres and upon illumination.<sup>30–32</sup> Also, large variability of the photoluminescence (PL) wavelength for MAPbI<sub>3</sub> films has been reported, indicating that the mechanisms leading to these changes are not well understood yet.<sup>33</sup> Shifts of the PL peak up to 20 nm have been observed and related to grain size, either controlled by the substrate morphology<sup>20,34,35</sup> or by the synthesis for aggregated perovskite dots.<sup>36</sup> On the other hand, theoretical studies correlate the optical band gap, and therefore PL wavelength, mainly with the Pb–I–Pb bond angle and Pb–I bond length which could be controlled through the steric size of the molecular cation without altering the metal-halide chemistry.<sup>37,38</sup> The grain size or defects located at the surface of the grains are invoked to explain the large emission wavelength variation observed both in bulk and in films, though for different crystal size ranges, while theory points to modifications of the inorganic framework.

In this work perovskite films are grown on commonly used electron and hole injection layers: compact TiO<sub>2</sub>, poly(3,4-

polyethylenedioxythiophene):poly(styrene sulfonate) (PEDOT:PSS), commercial fluorine doped SnO<sub>2</sub> (FTO) and bare glass for comparison. MAPbI<sub>3</sub>:Cl films are compared with MAPbI<sub>3</sub> polycrystalline powder. Synchrotron X-ray diffraction is used for an accurate structural characterization of films and bulk samples. Micro-photoluminescence (PL) and micro-Raman are used for *in situ* monitoring of the optical properties' variation with irradiation power and time. First, we have identified the Raman and PL characteristics of unperturbed MAPbI<sub>3</sub> bulk powder and films at very low laser power and studied their evolution and transformation in room ambient conditions at increasing laser power. We find that the nature of the underneath substrate influences the properties of the MAPbI<sub>3</sub>:Cl films not only at the substrate–film interface as it is commonly believed, but also the structure, morphology and composition of the whole film, and thus the bulk properties of the film. The different behavior for MAPbI<sub>3</sub>:Cl on oxide and polymeric PEDOT:PSS layers is indicative of the influence of the nature of the substrate on the reactivity of the MAPbI<sub>3</sub>:Cl film and on the role of oxygen in the radiative recombination.

## 2. Experimental

### 2.1 Sample preparation

Glass and glass/FTO substrates were cleaned with soap and deionized water, followed by sonication in a mixture of acetone/ethanol (1 : 1 v/v) during 15 min. The cleaned substrates were further treated with a UV (ultraviolet)–O<sub>3</sub> lamp for 15 min. The TiO<sub>2</sub> compact layer was deposited on glass/FTO by spray pyrolysis at 450 °C using a solution of titanium diisopropoxidebis(acetylacetonate) solution (75% in 2-propanol, Sigma-Aldrich) diluted in ethanol (1 : 39 v/v) with compressed oxygen as the carrier gas. After spraying the precursor solution, the substrates were sintered on a hot plate for 5 min at 450 °C. Then, the hot plate was turned off, and the samples were left to cool down to room temperature. The PEDOT:PSS (Clevis P VP, Al 4083) layer was deposited by spin coating (3000 rpm during 60 s). Then, the films were annealed on a hot plate at 150 °C for 30 min.

To obtain the hybrid halide perovskite MAPbI<sub>3</sub>:Cl films, 100 μL precursor solution was prepared by mixing PbCl<sub>2</sub> and CH<sub>3</sub>NH<sub>3</sub>I (1 : 3 molar ratio) (Aldrich, used as received) in anhydrous dimethylformamide (DMF, 40% w/w) and spin coated in air by onto the substrates, previously heated at 70 °C during 10 min, and cured at 100 °C in an oven under air flow for 90 min. The film thickness of the MAPbI<sub>3</sub>:Cl films was around 550–700 nm as evaluated by profilometry (Fig. S2†). Also, for comparison, bulk MAPbI<sub>3</sub> powder was prepared by mixing 461 mg of PbI<sub>2</sub> and 158.9 mg of MAI and grinding in an Agatha mortar. The color changed immediately obtaining MAPbI<sub>3</sub> as a brown–black powder.

### 2.2 Characterization techniques

The room temperature micro-photoluminescence (PL) and micro-Raman spectra were measured using the 488 nm excitation wavelength of an Ar<sup>+</sup> laser in backscattering geometry with

an Olympus microscope, a “super-notch-plus” filter from Kaiser and a Jobin-Yvon HR-460 monochromator coupled to a Peltier cooled Synapse CCD. The light was collected from 0.8  $\mu\text{m}$  or 4.5  $\mu\text{m}$  diameter spots (corresponding to  $\times 100$  and  $\times 20$  objectives). Different neutral optical filters were used to avoid damaging the samples. The laser power values used were then: 6  $\mu\text{W}$ , 50  $\mu\text{W}$ , 100  $\mu\text{W}$  or 4 mW. *In situ* PL measurements associated with Raman spectra were taken using the minimum output power density (6  $\mu\text{W}$ , 12  $\text{W cm}^{-2}$ ). The Raman and photoluminescence experiments were conducted in air at room conditions with an average relative humidity around 50%.

Synchrotron X-ray diffraction data were collected on a six-circle diffractometer (15 keV; 0.826  $\text{\AA}$ ) at the BM25B (SpLine) beamline at the European Synchrotron facility (ESRF), for films deposited on the different substrates and for a powder sample at RT. A constant dry nitrogen flux was maintained on the samples to avoid possible degradation of the samples under X-ray radiation in air. The six-circle diffractometer allowed the measurement of different configurations: (i) the standard  $\theta$ - $2\theta$  configuration with the transferred momentum perpendicular to the substrate; and (ii) in a geometry which reveals the in-plane order. In this latter case, the incident angle is fixed to  $2^\circ$  and the detector is scanned in the horizontal plane so that the transferred momentum has its larger component in the substrate plane. Diffraction maxima were fitted using a Voigt function starting from the instrumental resolution values for the profile parameters. These starting values were obtained by fitting data obtained for a powder Si standard reference supplied by NIST. The background was modeled by use of a twelve coefficient polynomial function. Lattice parameters were refined by the profile matching (Le Bail fit) procedure using the FullProf program integrated in the WinPLOTR software.<sup>39</sup> The average crystallite size was calculated using the Scherrer formula. The width (in transferred momentum) of the diffraction maxima of the same family was constant for each film for the whole measured range so strain effects are discarded.

Even though MAPbI<sub>3</sub> is a highly reactive material at room conditions, which may lead to its degradation resulting in the quenching of the PL emission, in suitable conditions (very low incident laser power) the qualitative evolution of the emission and Raman spectra upon illumination or in dark are reproducible for films prepared on the same substrate and over different places for each films. AFM and diffraction experiments are totally reproducible.

### 3. Results and discussion

#### 3.1 Morphology and crystal structure

To establish the correlation between the characteristics of the underlying substrate layer and those of MAPbI<sub>3</sub>:Cl film (as grain size, crystal size and optical properties) a morphological and structural study is required. The morphology of the four substrates (glass, glass/FTO, glass/FTO/PEDOT:PSS and glass/FTO/TiO<sub>2</sub>) has been analyzed by atomic force microscopy (AFM) (Fig. S1†) and that of MAPbI<sub>3</sub>:Cl films by optical microscopy and contact profilometry (Fig. S2†). The average roughness measured by AFM in the substrates was: 3.2, 15.3, 0.8 and

6.8 nm for bare glass, FTO, PEDOT:PSS and TiO<sub>2</sub> respectively. The thicknesses of the MAPbI<sub>3</sub>:Cl films were 650, 650, 550, and 750 nm for the film grown on glass, glass/FTO, glass/FTO/PEDOT:PSS, and glass/FTO/TiO<sub>2</sub>, with roughness of 156, 143, 116 and 126 nm, respectively.

The lattice parameters, preferential orientation and domain size were obtained for the MAPbI<sub>3</sub>:Cl films on the four substrates and compared to the MAPbI<sub>3</sub> powder (bulk) sample. The MAPbI<sub>3</sub> powder pattern was fit within the non-centrosymmetric *I4cm* space group (in ESI Fig. S3 and Table S1†) and the same group was used for the films (Fig. S4 and S5 in the ESI†). The films show a very strong preferential orientation in the  $\langle 110 \rangle$  direction as evidenced by comparing the relative intensities of the different reflections with those of the powder sample (Fig. 1a), and in particular of (004) and (220) maxima (Fig. S5†). The tetragonal symmetry of MAPbI<sub>3</sub> perovskite can be approximated to a pseudocubic one where the correlation of the lattice parameters with the tetragonal description is as follows:  $a_{\text{pc}} = b_{\text{pc}} = a_{\text{t}}/\sqrt{2} = b_{\text{t}}/\sqrt{2}$  and  $c_{\text{pc}} = c_{\text{t}}/2$ , inset of Fig. 1. Note that the tetragonal (004) and (220) reflections result from the splitting of the (200) reflection in the pseudocubic perovskite representation.

It can be seen that the intensity of all diffraction peaks with high *l* index (as 004, 213, 114, 204 or 224) are depleted,

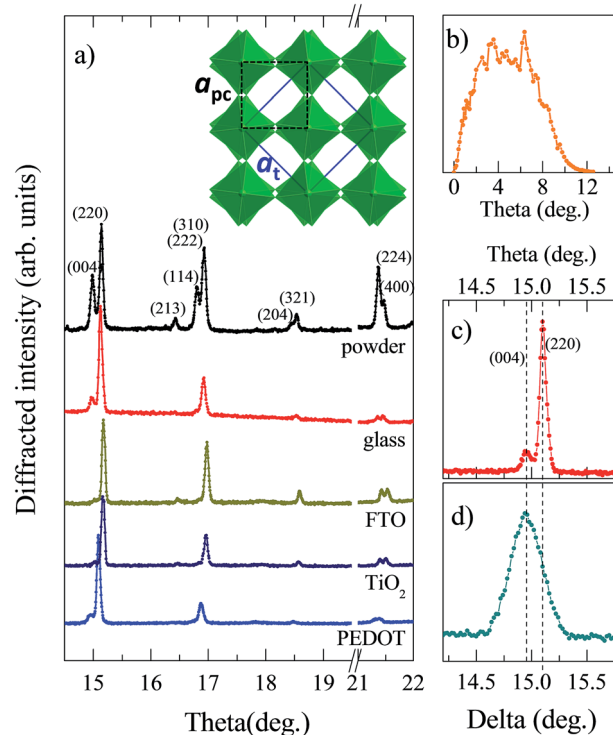


Fig. 1 (a) Synchrotron X-ray (15 keV = 0.826  $\text{\AA}$ ) patterns of MAPbI<sub>3</sub>:Cl films on glass (red), glass/FTO (FTO; olive), glass/FTO/TiO<sub>2</sub> (TiO<sub>2</sub>; dark blue), glass/FTO/PEDOT:PSS (PEDOT; blue) and MAPbI<sub>3</sub> powder (black) for comparison. The allowed Bragg reflections in the *I4cm* space group are indicated, (b) (220) rocking curve of MAPbI<sub>3</sub> on glass, (c) zoom of the  $\theta$ - $2\theta$  scan of MAPbI<sub>3</sub> on glass, and (d) of the  $\delta$  scan of MAPbI<sub>3</sub> on glass. Inset: crystal structure of MAPbI<sub>3</sub> on the *ab*-projection showing tetragonal and pseudocubic cells.

indicating not only the prevalence of the  $\langle 110 \rangle$  orientation but also that the  $c$ -axis tends to be contained in the substrate plane for any of the other orientations. The width of the rocking curve of the (220) reflection (Fig. 1b) indicates that the angular variation of the (220) grains around the surface normal is around  $4^\circ$ . To test the in-plane orientation of the film on glass we recorded the diffracted intensity in a configuration with the transferred momentum almost parallel to the surface with a fixed incident angle ( $2^\circ$ ) and scanning the detector angle ( $\delta$ ) in the sample plane (Fig. 1d). The comparison of this scan to the standard  $\theta$ - $2\theta$  scan (Fig. 1c) clearly shows that the (004) grains, and therefore the  $c$  axis, are parallel to the substrate.

The crystallite sizes for the differently oriented grains ( $D_{hkl}$ ) shown in Fig. 2a are obtained from the full width at half maximum (FWHM) of the corresponding reflections. The results show that the sizes of the  $\langle 110 \rangle$  oriented grains ( $D_{220}$ ) are significantly larger than the average of the other orientations ( $\langle D \rangle$ ) indicating a growth habit along  $[110]$  tetragonal direction which corresponds to the  $[100]_{pc}$  pseudocubic axis, and this behavior is enhanced in the films, especially when deposited on bare glass. The ratio between the integrated intensity of the 220 reflection and the total integrated intensity between  $14.5^\circ$  and  $19.5^\circ$  in two-theta (the definition is detailed in the ESI†) provides an estimation of the  $\langle 110 \rangle$  preferred orientation degree which also indicates the random-oriented grain fraction of the  $\text{MAPbI}_3\text{:Cl}$  films. The  $\langle 110 \rangle$  preferred orientation fraction reaches its maximum for the PEDOT:PSS substrate.

A very important conclusion of this study is that the lattice parameters of the  $\text{MAPbI}_3\text{:Cl}$  films are found to be sensitive to the substrate, see Fig. 2b. The obtained changes in lattice parameters indicate that the Pb–Pb distance varies by around

0.7% for the film on PEDOT:PSS compared to that on FTO. The use of synchrotron radiation has allowed an accurate determination of the lattice parameters, see Fig. 2b. Note that the variations reported from among different substrates are larger than the error bars. The substrate dependence of the pseudocubic lattice parameters is depicted in Fig. 2c. The presence of an oxide substrate (FTO or  $\text{TiO}_2$ ) produces a shrinking of both parameters ( $a_{pc}$  and  $c_{pc}$ ) compared to those in bulk, while for that of PEDOT:PSS layer below, with a quite different chemical nature, an increase. A physical origin of this dependence (strain imposed by the substrate) is not especially expected for these quite large  $\text{MAPbI}_3\text{:Cl}$  crystalline domains (from 80 to 140 nm) since no epitaxial growth is occurring. We therefore propose that the chemical nature and reactivity (related to the roughness and density of the underneath layer) of the substrate is modifying the lattice parameters more probably by varying the chloride content as well as by the incorporation of oxygen and iodine vacancies in the  $\text{MAPbI}_3\text{:Cl}$  films during the synthesis.

Within each film, the crystallite size measured by diffraction is different depending on its crystallographic orientation relative to the substrate being larger for those grains  $[110]$  oriented (or  $[100]$  and  $[010]$  in the pseudocubic representation as shown in the inset of Fig. 1) for all substrates. The average crystal sizes vary in a range from 40 to 140 nm and the prevalence of (110) grains increases on smoother substrates. The (110) preferential orientation growth of  $\text{MAPbI}_3\text{:Cl}$  on  $\text{TiO}_2$  (anatase) has been reported to be related to a higher binding energy between  $\text{MAPbI}_3\text{:Cl}$  (110) and  $\text{TiO}_2$  (101) surfaces compared to that of the other orientations. The higher binding energy is calculated to be due to the better structural matching between rows of adjacent perovskite halides and  $\text{TiO}_2$  under-coordinated titanium atoms due to the octahedral tilting in  $\text{MAPbI}_3$ .<sup>40</sup> However the

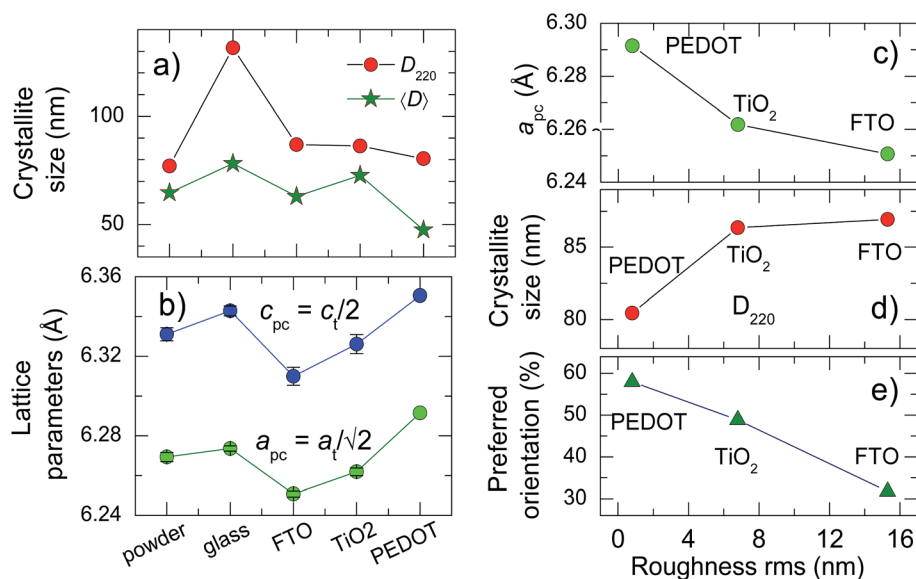


Fig. 2 (a) Variation of the crystallite size for  $\text{MAPbI}_3\text{:Cl}$  on glass, glass/FTO, glass/FTO/ $\text{TiO}_2$ , glass/FTO/PEDOT:PSS and  $\text{MAPbI}_3$  powder, for crystals in the  $\langle 110 \rangle$  direction (red circles) and the average value for the other directions (green stars), (b) pseudocubic lattice parameters ( $a_{pc}$  and  $c_{pc}$ ) of  $\text{MAPbI}_3\text{:Cl}$  for this series, (c) substrate roughness dependence of the pseudocubic lattice parameter  $a_{pc}$ , (d) of the crystal size for (110) grains and (e) of preferred orientation.

present results indicate that this preferential orientation occurs for any of the evaluated substrates which are polycrystalline or even amorphous and thus do not present a defined orientation. When no epitaxy can occur between the film and the substrate, as it is the case, the denser planes usually grow parallel to the substrate. In *fcc* structures this corresponds to (111) planes or in *hcp* to (001), but here, using the pseudocubic representation, the grains are (100) oriented, which is not denser. This is therefore an intrinsic and specific characteristic of MAPbI<sub>3</sub>. In a cubic perovskite the [100], [010] and [001] directions are totally equivalent and, in the distorted pseudocubic MAPbI<sub>3</sub> perovskite, these are also very similar directions. To explain the prevalence of (100)<sub>pc</sub> grains we propose that, since the film grows directly from a solution onto the substrate, the driving force for the grain alignment may be the only strongly non isotropic component which is the axial the MA<sup>+</sup> molecule. The CN-methylammonium bond axis, in the non-centrosymmetric *I4cm* space group, is along the [001] direction which, for the (110) grains, lies in the perovskite–substrate interface. In this case we can understand that the substrate roughness is an important factor for the fraction of the (110) oriented grains, as evidenced in our results. The key point may rather be related to the orientation of MA cations on the surface. Moreover, the preferential (110) fraction is found to increase as the roughness of the underneath layer is reduced (Fig. 2d) indicating also that the interface morphology and chemical nature are playing a role in the nucleation and growth of the MAPbI<sub>3</sub>:Cl grains. The crystal size for (110) grains (Fig. 2d) also shows a monotonous dependence on the roughness of the substrate with smaller crystals as their prevalence increases (Fig. 2e). Previously we have reported that preferential orientation of perovskite layer is also influenced by the presence of a scaffold.<sup>41</sup>

### 3.2 Photoluminescence and Raman analysis

The measured steady state PL band maximum lies within in a close range, 775.5–779 nm, for MAPbI<sub>3</sub>:Cl films on the different substrates exciting at 488 nm laser wavelength with very low power (6 μW, 12 W cm<sup>-2</sup>) (left panel of Fig. S6†) which corresponds well to the reported MAPbI<sub>3</sub> emission.<sup>42</sup> We did not observe a large difference in the PL wavelength for the films, contrary to the large variations reported before.<sup>20,34,36</sup> The measured PL wavelengths do not correlate to the observed lattice parameters, which are directly related to the Pb–Pb interatomic distances. The homogeneity of the PL intensity for the different samples has been checked by micro-PL images within 20 × 20 μm size areas (right panel Fig. S6†). The most uniform emission is for the films on PEDOT:PSS and TiO<sub>2</sub> even if their roughness is very different (0.8 and 6.8 nm). The structural and morphologic diversity of the films does not have an important impact on the PL since we find that the small changes in the emission peaks are not related to crystal size, within the 40–140 nm range, to substrate roughness up to around 16 nm or to obtained small variations of lattice parameters. Theoretical studies predict a variation of around 0.02 eV per degree for the band gap energy with the Pb–I–Pb angle.<sup>37,38</sup> Assuming that the major effect derived from the

observed lattice parameter variation (around 0.7%) is due to the change in Pb–I–Pb angles maintaining Pb–I bond lengths, a change in the band gap of 0.02 eV (10 nm), larger than that observed (3 nm), is expected. However experimental data for hybrid SnI<sup>37</sup> perovskites show variations in the 0 to 2 nm range for equivalent angle change. Therefore the observed wavelength shifts are more probably influenced by the presence of defects since substitutional Cl and oxygen and I vacancies may induce local modifications of the exciton binding energies.

**3.2.1. Bulk perovskite.** To study the influence of the emission properties of different parameters on MAPbI<sub>3</sub>:Cl films, such as their morphology or environmental and substrate effects in devices, it is important to identify undoubtedly the possible degradation residues. These halide perovskites present low energy formation and therefore also require low energy to separate the perovskite solid into ions during operation.<sup>9</sup> The laser itself and ambient conditions can induce degradation that may lead to misinterpretation because the Raman signal from the perovskite can be much lower than that of precursor compounds and/or degradation products. In addition the kind of degradation observed depending on the substrate can provide important information on the influence of the substrate in the film bulk properties. Raman spectra at different laser powers were collected and compared with the spectra of possible residues generated upon light irradiation.

The Raman spectra, obtained with a 488 nm excitation wavelength, for bulk MAPbI<sub>3</sub> and for relevant related compounds (PbO<sub>2</sub>, PbI<sub>2</sub> and MAI) are shown in Fig. 3 in the low frequency range up to 350 cm<sup>-1</sup>, left panels, and in an extended range, right panels. In Fig. 3a, the olive line corresponds to the PbO<sub>2</sub> spectrum. In Fig. 3b, orange lines are the spectra of the pressed PbI<sub>2</sub> pellet and small crystals present on the surface at low laser power (50 μW, 2.5 kW cm<sup>-2</sup>) while olive lines are those measured with high power (4 mW, 200 kW cm<sup>-2</sup>). PbI<sub>2</sub> has an energy gap typically of 2.5 eV<sup>43</sup> and is therefore Raman resonant under 488 nm (2.54 eV) excitation. In this situation the intensity of the peak around 210 cm<sup>-1</sup> (assigned to a two-phonon mode) is enhanced compared to the first order Raman modes around 110–120 cm<sup>-1</sup>, this peak not being observable out of resonance. The broad band detected at 770 cm<sup>-1</sup> in the Raman shift (right panel) is more probably due to the exciton emission (2.45 eV) close to the bandgap of PbI<sub>2</sub>. The spectra are totally modified when increasing the laser power from 50 μW to 4 mW. In this case the observed spectra correspond to lead oxide, similar to that shown in Fig. 3a. Different lead oxides can be formed (PbO, PbO<sub>2</sub>, Pb<sub>3</sub>O<sub>4</sub>) but all show a characteristic peak in the range 135–140 cm<sup>-1</sup>.<sup>44,45</sup> In the present case the peak at 138 cm<sup>-1</sup> and the presence of the two-phonon peak around 278 cm<sup>-1</sup> indicate the transformation of PbI<sub>2</sub> into PbO<sub>2</sub>. This transformation is observed also for the films, as we will see below. Fig. 3c collects the spectra of MAI, which is a precursor of the synthesis. Beside the internal modes of MA detected at frequencies above 900 cm<sup>-1</sup>, a narrow Raman peak at 115 cm<sup>-1</sup> is more probably due to a MA mode. MAI is totally stable with laser power.

MAPbI<sub>3</sub> is well known to be very susceptible to laser power and to the atmosphere, in particular to humidity. At very low

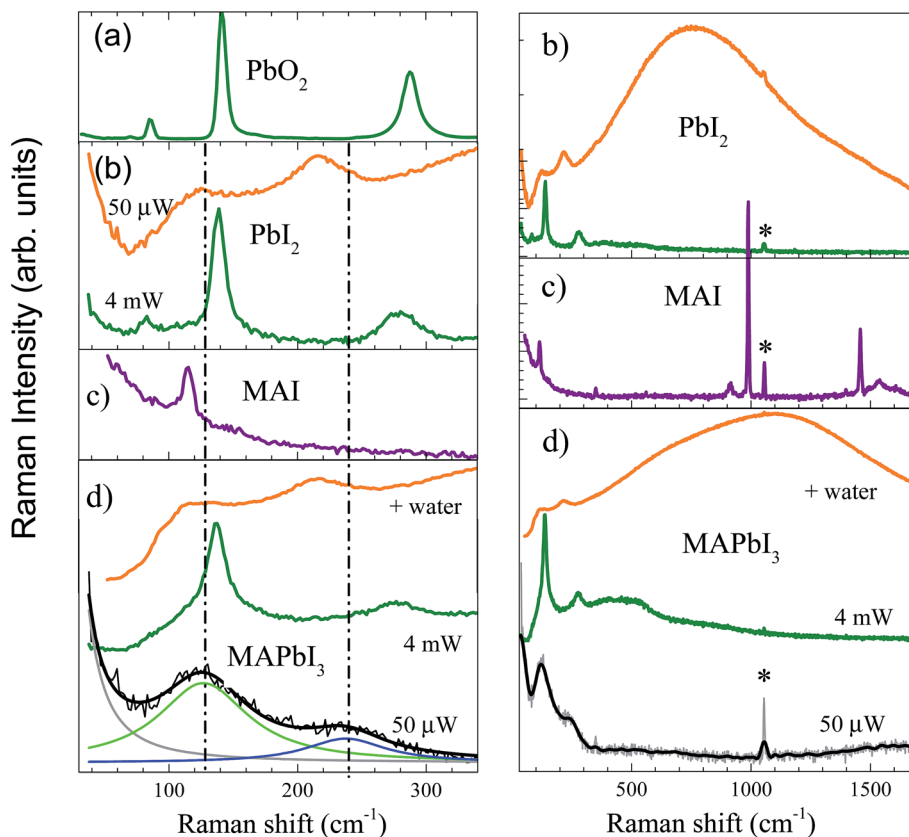


Fig. 3 Raman spectra obtained with 488 nm excitation at RT for low (left) and high (right) frequency ranges of (a)  $\text{PbO}_2$  (green line) and (b)  $\text{PbI}_2$  polycrystalline samples. Resonant Raman spectra obtained at low laser power (orange lines) showing the typical Raman modes (left panel) and emission of  $\text{PbI}_2$  (right panel) and, at high power (olive lines) show its transformation into  $\text{PbO}_x$ . (c) MAI (purple lines), (d) bulk  $\text{MAPbI}_3$  spectra at low laser power (black lines with their fit), high power (olive lines) showing the transformation into  $\text{PbO}_x$  and low power with water droplet (orange lines) showing the transformation into  $\text{PbI}_2$ . The vertical dash-dot lines signal the  $\text{MAPbI}_3$  Raman peaks (\* indicate laser plasma line).

laser power the obtained spectrum, plotted as black lines in Fig. 3d, is very well fitted to two Lorentz functions peaking at 127 and 237  $\text{cm}^{-1}$ . As the incident power is increased in a low humidity atmosphere (<40%) the spectrum is progressively modified, reaching the situation plotted in olive lines which clearly corresponds to  $\text{PbO}_2$ , as in the case of  $\text{PbI}_2$  measured at high power as previously described. In these conditions only the addition of a water droplet produces the transformation to  $\text{PbI}_2$  (orange spectra) showing both Raman modes and the luminescence band. In any of these situations, the transformation of  $\text{MAPbI}_3$  into  $\text{PbI}_2$  or  $\text{PbO}_x$ , the intense characteristic PL emission band of  $\text{MAPbI}_3$  perovskite around 775 nm vanishes. Raman peaks in the range 135–140  $\text{cm}^{-1}$  undoubtedly indicate the formation of  $\text{PbO}_x$ . The experimental frequencies obtained here for the different compounds are summarized in Table S2 in the ESI,<sup>†</sup> together with some reported experimental and calculated values. The observed  $\text{MAPbI}_3$  band around 127 and 237  $\text{cm}^{-1}$  is associated with  $\text{MA}^+$  libration and torsional modes, respectively. The discussion of assignment is detailed in the ESI.<sup>†</sup>

This extreme susceptibility of  $\text{MAPI}_3$  and the large width of the bands makes it difficult to extract information from the Raman spectra for these compounds. A key question is why

Raman peaks are so poorly defined. On one hand the bandgap of  $\text{MAPbI}_3$  (around 1.6 eV) is smaller than most of the laser excitation energies used for Raman spectroscopy, therefore the high absorption and the use of highly focused beams produces important local heating of the samples. In our case we monitored the stability of the 775 nm characteristic PL emission and associated Raman spectra to elucidate if any transformation of the sample was occurring. Nevertheless, the actual temperature of the sample at the laser spot may be increased and, since  $\text{MAPbI}_3$  suffers a structural transition at only around 30 °C above RT, the sample can transit to the high temperature phase. In this case, the Raman modes may differ from those of the RT tetragonal  $I4cm$  phase. Nevertheless a small temperature increase does not justify the observed large peak width. Above 160 K the  $\text{MA}^+$  ions are tumbling within the inorganic cage.<sup>46</sup> These movements induce a dynamic disorder in the Pb–I octahedra which, through the coupling between MA and Pb–I octahedra, will influence the MA libration and torsional modes. This situation can be paralleled to the effect of polaron hopping in doped manganese perovskites (as  $\text{La}_{1-x}\text{Ca}_x\text{MnO}_3$ ) in the paramagnetic phase. We reported that the hopping electron induces a dynamical Jahn–Teller distortion of the perovskite structure so that wide poorly defined Raman peaks are

detected.<sup>47</sup> We therefore propose that the Raman peak width is related to the dynamical deformations induced by MA tumbling in the tetragonal and cubic or pseudocubic phases.

**3.2.2. Films on different substrates.** Similar formation of  $\text{PbO}_x$  lead oxide are observed also for the films on glass (Fig. 4), FTO and FTO/ $\text{TiO}_2$  substrates (Fig. S7†). The identification of these peaks to  $\text{PbO}_x$  is crucial, since some authors reported the 140 and 270  $\text{cm}^{-1}$  peaks as  $\text{MAPbI}_3$  phonons.<sup>32</sup> Recently Kong *et al.*<sup>48</sup> reported that oxygen intercalation into the frameworks of  $\text{MAPbI}_3$  induced by photocatalysis on the surface induces this 140  $\text{cm}^{-1}$  peak. In fact, however, this peak is more probably related to the partial transformation of  $\text{MAPbI}_3$  into  $\text{PbO}_x$ , as the PL emission is quenched. Also, some authors associate the 140  $\text{cm}^{-1}$  peak with the  $\text{TiO}_2$  buffer layer.<sup>49</sup> The usually small thickness of  $\text{TiO}_2$  layers in devices, the nanosize of the particles, their uncertain ordering and the strongly absorbing  $\text{MAPbI}_3$  overlayer, however, make improbable the detection of Raman  $\text{TiO}_2$  modes. Therefore, in this case also these bands indicate the formation of  $\text{PbO}_x$ . As far as we know there is no assignment to  $\text{PbO}_x$  phases in previous works.

The perovskite film has been intentionally degraded by increasing progressively the laser illumination power to obtain information about the nature of defects in the different samples analyzed. The Raman spectra obtained at different laser power and the PL recorded at a very low constant laser power (6  $\mu\text{W}$ , 0.3  $\text{kW cm}^{-2}$ ) from the same location in the sample were obtained for the films on the four different substrates (Fig. 4 and S7†). In

Fig. 4 we can observe the Raman spectra for the perovskite film on glass with increasing incident power laser and their associated PL emission. At the lowest power (stage 1) the spectrum is similar to that of bulk  $\text{MAPbI}_3$  but in stage 2 quite sharp peaks at 110 and 165  $\text{cm}^{-1}$  are detected concomitantly to a significant PL intensity increase (Fig. 4b). In stages 3 and 4 the PL decrease coincides with the appearance and increase of a peak at 138  $\text{cm}^{-1}$ , which we previously demonstrated to be the fingerprint of the formation of  $\text{PbO}_x$ , see Fig. 3. Finally in stage 5 the PL peak disappears completely (not shown) and major transformation to  $\text{PbO}_x$  within the laser spot occurs. Intermediate stage 2 is especially interesting since an enhancement of PL intensity is occurring, see Fig. 4b. Light-induced halide migration has been reported to occur in metal halides such as  $\text{PbBr}_2$  and  $\text{PbI}_2$ .<sup>50,51</sup> Also, halide vacancies and halide migration are energetically probable in hybrid halide perovskites.<sup>52,53</sup> Thus, in this stage 2, the Raman modes at 110 and 165  $\text{cm}^{-1}$  may be activated by the presence of different type of defects as halide vacancies and the incorporation of oxygen into these vacancies of the  $\text{MAPbI}_3$  structure. Nevertheless halide vacancies are required for charge neutrality compensation of  $\text{O}^{2-}$ , therefore a certain concentration of vacancies will be present. The evolution of Raman spectra is similar for the films in all substrates except that for PEDOT:PSS where  $\text{PbO}_x$  phase cannot be identified, see Fig. S7.† Also the transformation degree for a given laser power is not identical for the four films.

It is important to highlight that the Raman spectra originate from the top part of the perovskite film, as the absorption depth for the employed excitation wavelength (488 nm) is around 85 nm (much smaller than the film thicknesses) calculated from reported absorption coefficient.<sup>54</sup> Consequently the light induced observed changes do not originate in the perovskite/substrate interface but in the bulk of the film. Nevertheless, the different behavior observed for samples grown on oxide or on PEDOT:PSS substrates, see Fig. S7.† are explained by the influence of the substrate in the nucleation and growth of the film, not only in terms of structure and morphology but also regarding the type and relative content of point defects. So, the chemical nature of bulk  $\text{MAPbI}_3$  is indeed affected by the substrate, which plays an important role in light-induced modification.

Fig. 5 summarizes the evolution of the corresponding PL band at each Raman stage (obtained after recording the Raman spectra at the same position with very low laser power) for the four films. Only small changes are detected in the PL wavelength and FWHM but the intensity does significantly vary. Associated to the appearance of Raman peaks related to the incorporation of oxygen, and possibly also of vacancies as mentioned above, (stages 2 and 3), the PL intensity increases and reaches its maximum value either in stage 2 or 3 depending on the substrate. In stage 4, when the transformation to  $\text{PbO}_x$  is evidenced in Raman spectra, the PL intensity decreases. We propose that the intensity increase in stages 2 and 3 can be related to e-h exciton localization by the photo-induced defects. The localization of the excitons would enhance the radiative recombination probability by hindering charge mobility. The

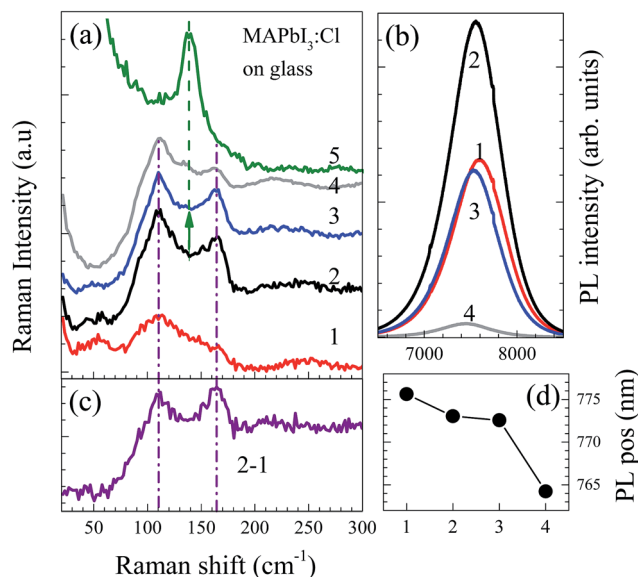


Fig. 4 (a) Raman spectra of  $\text{MAPbI}_3:\text{Cl}$  film on glass at low power incident light (1, red line) and increasing laser power: (1) = 50  $\mu\text{W}$  (2.5  $\text{kW cm}^{-2}$ ), (2) = 100  $\mu\text{W}$  (5  $\text{kW cm}^{-2}$ ), (3) = 1 mW (44  $\text{kW cm}^{-2}$ ), (4) = 3 mW (130  $\text{kW cm}^{-2}$ ) and (5) = 4 mW (200  $\text{kW cm}^{-2}$ ), respectively; and (b) corresponding PL emission obtained at a constant low laser power, 6  $\mu\text{W}$  (0.3  $\text{kW cm}^{-2}$ ), just after recording the Raman spectra; (c) difference of Raman spectra 1 and 2; and (d) evolution with irradiation of the PL wavelength for the 4 stages. Purple lines indicate the emerging peaks of the intermediate stage at 110 and 165  $\text{cm}^{-1}$  and the green line and arrow the final  $\text{PbO}_x$  stage.

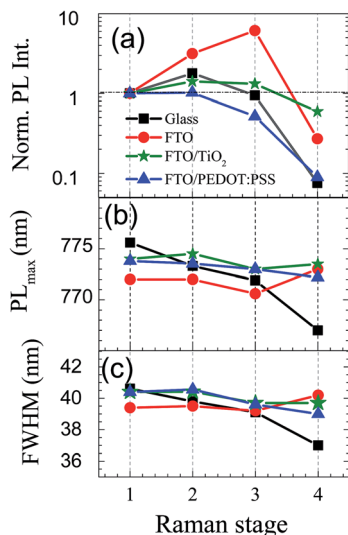


Fig. 5 Evolution of the corresponding PL at each Raman stage induced by increasing incident laser power. (a) Evolution of the PL intensity normalized at the initial state, (b) wavelength and (c) FWHM.

different behavior for  $\text{MAPbI}_3:\text{Cl}$  on the polymeric PEDOT:PSS layer, where increasing the incident power does not produce an increase in PL intensity, is indicative again of the influence of the nature of the substrate on the final properties of the perovskite film.

At the lowest incident laser power it is apparent that the Raman spectra of the samples do not evolve, but after a sufficient time the laser beam illuminating the samples can induce stage 2, and PL shows changes over time. Upon illumination, the PL emission of  $\text{MAPbI}_3:\text{Cl}$  films again exhibits different effects for the different substrates, despite the fact that the excitation light is absorbed on the top of the perovskite layer, far from the substrate. Fig. 6 shows the evolution of the PL wavelength, full width and intensity normalized to the initial state at different times under illumination of  $6 \mu\text{W}$  ( $12 \text{ W cm}^{-2}$ ) 488 nm laser light (solid symbols) and dark conditions (open symbols). Black square for glass, red circles for FTO, green stars for  $\text{TiO}_2$  and blue triangles for PEDOT:PSS.

Studies of the PL properties in air, nitrogen, and an oxygen/helium environment suggest that oxygen is important for PL enhancement.<sup>56</sup> In fact, the role of oxygen is supported by the fact that the PL intensity decreases upon white illumination in an  $\text{N}_2$  environment.<sup>55,55,57</sup> PL intensity enhancement upon illumination in ambient conditions has been reported and tentatively explained by a catalytic reaction induced by oxygen in inorganic  $\text{SrTiO}_3$  thin film perovskite.<sup>58</sup> Other studies reported diverse behavior of the photoluminescence of  $\text{MAPbI}_3:\text{Cl}$  upon light irradiation. A slow rise of the PL over a time scale of

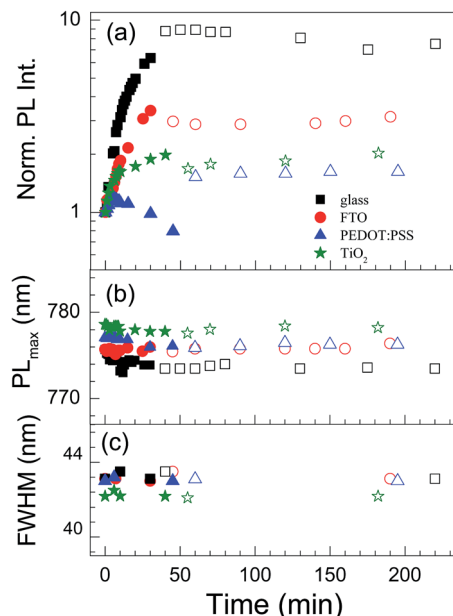


Fig. 6 (a) Evolution of the PL intensity normalized to the initial state measured at very low incident laser power ( $6 \mu\text{W}$ ,  $12 \text{ W cm}^{-2}$ ), (b) PL wavelength, and (c) full width at half maximum (FWHM) over times up to 4 hours for the films on the four substrates, under illumination of 488 nm laser light (solid symbols) and dark conditions (open symbols). Black square for glass, red circles for FTO, green stars for  $\text{TiO}_2$  and blue triangles for PEDOT:PSS.

seconds<sup>59</sup> has been associated with the passivation of gap states acting as subgap nonradiative pathways. Nevertheless, most defects are shallow traps and are therefore not expected to act as non-radiative decay paths.<sup>60,61</sup> At longer irradiation times (minutes) a PL enhancement, and lifetime increase from nanoseconds to hundreds of nanoseconds, has been observed<sup>62</sup> and associated with de-activation by a photochemical reaction involving the oxygen of trapping sites responsible for non-radiative charge recombination. Which are the initial traps and where the oxygen incorporates is not clarified. On the other hand, Shi *et al.*<sup>63</sup> calculated the defect states involving oxygen, suggesting that small  $\text{O}^{2-}$  ions for  $\text{I}^-$  vacancy replacement is feasible. The calculations are compatible with the here-proposed scenario in which laser illumination and oxygen presence induces the incorporation of oxygen and the presence of iodine vacancies and substitutional  $\text{Cl}^-$  with different concentrations depending on the substrate. The samples with more stable behavior over time, films on  $\text{TiO}_2$  and FTO, can obtain oxygen diffused through the surface and from the layer below, contrary to the film on glass. Consequently the substrate-induced changes in the  $\text{MAPbI}_3:\text{Cl}$  film structure, more probably originated by different concentrations of defects (likely to be substitutional Cl, oxygen or vacancies), and the nature of the substrate determines the emission properties and the sensitivity to light. Ambient oxygen is a relevant factor in the observed PL enhancement associated with stage 2, and the peaks at 110 and  $165 \text{ cm}^{-1}$  observed in Raman spectra could be indicative of its incorporation. Our results provide important insights in the importance of the nature of the substrate on the

bulk properties of halide perovskite grown on its top, aim to provide important clues to the working mechanism of PSCs and point to optimization of the performance of perovskite based optoelectronic devices.

## 4. Conclusions

In summary, we have shown that the substrate influences the bulk properties of MAPbI<sub>3</sub>:Cl films by a systematic structural and optical characterization of perovskite films grown on glass, glass/FTO, glass/FTO/PEDOT:PSS and glass/FTO/TiO<sub>2</sub> substrates. The perovskite films present a strong preferential orientation in the <110> direction for any of the evaluated substrates. The preferential (110) fraction is found to increase as the roughness of the substrate is reduced, indicating that the interface morphology is playing a role in the nucleation and growth of the MAPbI<sub>3</sub>:Cl grains. The key point may be related to the orientation of the CN–methylammonium bond axis at the MAPbI<sub>3</sub>:Cl–substrate interface which is parallel to the substrate for the (110) grains in the non-centrosymmetric *I4cm* space group. The average crystal sizes vary in a range from 40 to 140 nm and the prevalence of (110) grains increases on smoother substrates. Besides, the chemical nature and reactivity of the substrate is also modifying the lattice parameters by varying the chlorine content as well as by the incorporation of oxygen and probably iodine vacancies in the MAPbI<sub>3</sub>:Cl films during the synthesis. The obtained changes in the lattice parameter indicate that the Pb–Pb distance varies by around 0.7%.

Low frequency Raman modes of bulk and films are broad peaks around 127 cm<sup>-1</sup> (MA libration) and 237 cm<sup>-1</sup> (MA torsional mode) and their widths are related to dynamical deformations of the Pb–I octahedra induced by MA tumbling. Light induces the progressive modification of the perovskite up to its transformation into PbO<sub>x</sub> revealed by Raman peaks at around 138 and 270 cm<sup>-1</sup> besides PL quenching. The addition of water is required for its transformation into PbI<sub>2</sub> (110 and 220 cm<sup>-1</sup> Raman peaks). A different behavior for MAPbI<sub>3</sub>:Cl films grown on oxide layers (TiO<sub>2</sub> and FTO) is observed compared to that on PEDOT:PSS polymer where PbO<sub>x</sub> is not detected. An intermediate stage shows quite sharp peaks at 110 and 165 cm<sup>-1</sup> concomitant with a significant PL intensity increase in all substrates except on PEDOT:PSS. These Raman peaks may be activated by the presence of defects as a result of oxygen incorporation and halide vacancies.

A non reversible increase of PL with illumination time has been observed for samples on oxide substrates but not for those on the polymer substrate. The intensity increase can be related to the localization of a fraction of the electron–hole excitons by the photo-induced defects enhancing the radiative recombination by hindering charge mobility. The different behavior for MAPbI<sub>3</sub>:Cl on the PEDOT:PSS layer is indicative of the influence of the nature of substrate on the reactivity of MAPbI<sub>3</sub> films and the role of oxygen in the radiative recombination rate.

The mechanism that we propose for the observed changes in the structure, crystal size and preferential orientation of the perovskite films as a function of the substrate are due mainly to

the roughness of the surface but also to its chemical nature. The substrate roughness is a key factor in the morphology of the perovskite grains but also in the concentration of defects (substitutional Cl, oxygen and vacancies) by providing a different density of nucleation sites and grain growth dynamics. On the other hand, the different behavior with illumination time and power of the films synthesized on a polymeric substrate (PEDOT) compared to the inorganic oxide ones (TiO<sub>2</sub>, glass and FTO) indicate that the chemical nature of the substrate is playing a role in the relative concentrations of the point defects. These defects originate within the perovskite film structure during growth, which in turn gives rise to different types of degradation and modification with illumination. We also demonstrate the influence of the nature of the substrate on the reactivity of the MAPbI<sub>3</sub> film and the role of oxygen in the radiative recombination rate.

This work highlights how the substrate influences not just the interfacial properties of perovskite devices but also the bulk perovskite properties, a fact with important implications on the PSC working mechanisms. In this sense, major implications on the solar cell performance can be anticipated from the substrate choice and these will have important implications for device optimization.

## Acknowledgements

Funding by the Spanish Ministerio de Economía y Competitividad (MINECO) under Projects MAT2015-65356-C3-1-R and 2-R, MAT2014-54852-R and MAT2015-70611-ERC and Comunidad de Madrid Excellence Network under Project S2013/MIT-2740 (and Associated Lab LABCADIO belonging to CM net labs ref. 351) is acknowledged. We also acknowledge the MINECO for financial support and provision of synchrotron radiation facilities at ESRF, and thank María Vila for her assistance in using beamline BM25-SpLine. B. C. H. is grateful to the support of the National Council of Technological and Scientific Development (CNPq), Brazil, through the Science without Borders program.

## References

- 1 D. Weber, *Z. Naturforsch., B: J. Chem. Sci.*, 1978, **33**, 1443.
- 2 D. Weber, *Z. Naturforsch., B: J. Chem. Sci.*, 1978, **33**, 862.
- 3 A. Kojima, K. Teshima, Y. Shirai and T. Miyasaka, *J. Am. Chem. Soc.*, 2009, **131**, 6050.
- 4 H.-S. Kim, C.-R. Lee, J.-H. Im, K.-B. Lee, T. Moehl, A. Marchioro, S.-J. Moon, R. Humphry-Baker, J.-H. Yum, J. E. Moser, M. Grätzel and N.-G. Park, *Sci. Rep.*, 2012, **2**, 591.
- 5 M. M. Lee, J. Teuscher, T. Miyasaka, T. N. Murakami and H. J. Snaith, *Science*, 2012, **338**, 643–647.
- 6 Research Cell Efficiency Records, [http://www.Nrel.Gov/Ncpv/Images/Efficiency\\_Chart.Jpg](http://www.Nrel.Gov/Ncpv/Images/Efficiency_Chart.Jpg), accessed, February 2016.
- 7 T. C. Sum and N. Mathews, *Energy Environ. Sci.*, 2014, **7**, 2518–2534.
- 8 M. A. Green, A. Ho-Baillie and H. J. Snaith, *Nat. Photonics*, 2014, **8**, 506–514.
- 9 H. S. Jung and N.-G. Park, *Small*, 2015, **11**, 10–25.

- 10 Y. Zhao and K. Zhu, *J. Phys. Chem. Lett.*, 2014, **5**, 4175–4186.
- 11 M. A. Green, K. Emery, Y. Hishikawa, W. Warta and E. D. Dunlop, Solar cell efficiency tables (version 45), *Prog. Photovoltaics Res. Appl.*, 2015, **23**, 1–9.
- 12 J. Burschka, N. Pellet, S. J. Moon, R. Humphry-Baker, P. Gao, M. K. Nazeeruddin and M. Grätzel, *Nature*, 2013, **499**, 316–319.
- 13 G. E. Eperon, V. M. Burlakov, P. Docampo, A. Goriely and H. J. Snaith, *Adv. Funct. Mater.*, 2014, **24**, 151–157.
- 14 B. Chen, M. Yang, S. Priya and K. Zhu, *J. Phys. Chem. Lett.*, 2016, **7**, 905–917.
- 15 O. Almora, C. Aranda, I. Zarazua, A. Guerrero and G. Garcia-Belmonte, *ACS Energy Lett.*, 2016, **1**, 209–215.
- 16 W. Tress, N. Marinova, T. Moehl, S. M. Zakeeruddin, M. K. Nazeeruddin and M. Gratzel, *Energy Environ. Sci.*, 2015, **8**, 995–1004.
- 17 E. L. Unger, E. T. Hoke, C. D. Bailie, W. H. Nguyen, A. R. Bowring, T. Heumuller, M. G. Christoforo and M. D. McGehee, *Energy Environ. Sci.*, 2014, **7**, 3690–3698.
- 18 Y. Shao, Z. Xiao, C. Bi, Y. Yuan and J. Huang, *Nat. Commun.*, 2014, **5**, 5784.
- 19 F. K. Aldibaja, L. Badia, E. Mas-Marza, R. S. Sanchez, E. M. Barea and I. Mora-Sero, *J. Mater. Chem. A*, 2015, **3**, 9194–9200.
- 20 G. Grancini, S. Marras, M. Prato, C. Giannini, C. Quarti, F. De Angelis, M. De Bastiani, G. E. Eperon, H. J. Snaith, L. Manna and A. Petrozza, *J. Phys. Chem. Lett.*, 2014, **5**, 3836–3842.
- 21 P. Docampo, F. Hanusch, S. D. Stranks, M. Döblinger, J. M. Feckl, M. Ehrensperger, N. K. Minar, M. B. Johnston, H. J. Snaith and T. Bein, *Adv. Energy Mater.*, 2014, **4**, 1400355.
- 22 S. Colella, E. Mosconi, P. Fedeli, A. Listorti, F. Gazza, F. Orlandi, P. Ferro, T. Besagni, A. Rizzo and G. Calestani, *Chem. Mater.*, 2013, **25**, 4613–4618.
- 23 G. Xing, N. Mathews, S. Sun, S. S. Lim, Y. M. Lam, M. Gratzel, S. Mhaisalkar and T. C. Sum, *Science*, 2013, **342**, 344–347.
- 24 E. L. Unger, A. R. Bowring, C. J. Tassone, V. L. Pool, A. Gold-Parker, R. Cheacharoen, K. H. Stone, E. T. Hoke, M. F. Toney and M. D. McGehee, *Chem. Mater.*, 2014, **26**, 7158–7165.
- 25 T. Baikie, Y. Fang, J. M. Kadro, M. Schreyer, F. Wei, S. G. Mhaisalkar, M. Gratzel and T. J. White, *J. Mater. Chem. A*, 2013, **1**(18), 5628.
- 26 T. Baikie, N. S. Barrow, Y. Fang, P. J. Keenan, P. R. Slater, R. O. Piltz, M. Gutmann, S. G. Mhaisalkar and T. J. White, *J. Mater. Chem. A*, 2015, **3**, 9298–9307.
- 27 C. C. Stoumpos, C. D. Malliakas and M. G. Kanatzidis, *Inorg. Chem.*, 2013, **52**(15), 9019–9038.
- 28 F. Brivio, J. M. Frost, J. M. Skelton, A. J. Jackson, O. J. Weber, M. T. Weller, A. R. Goni, A. M. A. Leguy, P. R. F. Barnes and A. Walsh, *Phys. Rev. B: Condens. Matter Mater. Phys.*, 2015, **92**, 144308.
- 29 I. P. Swainson, C. Stock, S. F. Parker, L. Van Eijck, M. Russina and J. W. Taylor, *Phys. Rev. B: Condens. Matter Mater. Phys.*, 2015, **92**, 100303R.
- 30 C. Quarti, G. Grancini, E. Mosconi, P. Bruno, J. M. Ball, M. M. Lee, H. J. Snaith, A. Petrozza and F. De Angelis, *J. Phys. Chem. Lett.*, 2014, **5**, 279–284.
- 31 M. Ledinský, P. Löper, B. Niesen, J. Holovský, S.-J. Moon, J.-H. Yum, S. De Wolf, A. Fejfar and C. Ballif, *J. Phys. Chem. Lett.*, 2015, **6**, 401–406.
- 32 B. W. Park, S. M. Jain, X. Zhang, A. Hagfeldt, G. Boschloo and T. Edvinsson, *ACS Nano*, 2015, **9**, 2088.
- 33 D. W. de Quilettes, S. M. Vorpahl, S. D. Stranks, H. Nagaoka, G. E. Eperon, M. E. Ziffer, H. J. Snaith and D. S. Ginger, *Science*, 2015, **348**(6235), 683–686.
- 34 V. D'Innocenzo, A. R. S. Kandada, M. De Bastiani, M. Gandini and A. Petrozza, *J. Am. Chem. Soc.*, 2014, **136**, 17730–17733.
- 35 N. J. Jeon, J. H. Noh, Y. C. Kim, W. S. Yang, S. Ryu and S. I. Seok, *Nat. Mater.*, 2014, **13**, 897–903.
- 36 F. Zhu, L. Men, Y. Guo, Q. Zhu, U. Bhattacharjee, P. M. Goodwin, J. W. Petrich, E. A. Smith and J. Vela, *ACS Nano*, 2015, **9**(3), 2948–2959.
- 37 J. L. Knutson and J. D. Martin, *Inorg. Chem.*, 2014, **44**, 4699.
- 38 M. R. Filip, G. E. Eperon, H. J. Snaith and F. Giustino, *Nat. Commun.*, 2014, **5**(5), 5757.
- 39 J. Rodríguez-Carvajal and T. Roisnel, FULLPROF, WWINPLOTR, and accompanying programs, <http://www.ill.eu/sites/fullprof/index.html>, accessed May 2016.
- 40 E. Mosconi, E. Ronca and F. De Angelis, *J. Phys. Chem. Lett.*, 2014, **5**, 2619–2625.
- 41 A. Listorti, E. J. Juarez-Perez, C. Frontera, V. Roiati, L. Garcia-Andrade, S. Colella, A. Rizzo, P. Ortiz and I. Mora-Sero, *J. Phys. Chem. Lett.*, 2015, **6**, 1628–1637.
- 42 W. Kewei, A. Bera, C. Ma, Y. Du, Y. Yang, L. Li and T. Wu, *Phys. Chem. Chem. Phys.*, 2014, **16**, 22476–22481.
- 43 I. Baltog, M. Baibarac and S. Lefrant, *J. Phys.: Condens. Matter*, 2009, **21**(2), 025507.
- 44 U. Detlef, T. Wiechert, S. P. Grabowski and M. Simon, *Thin Solid Films*, 2005, **484**, 73–82.
- 45 L. Burgio, R. J. Clark and S. Firth, *Analyst*, 2001, **126**, 222–227.
- 46 A. Poglitsch and D. Weber, *J. Chem. Phys.*, 1987, **87**, 6373.
- 47 L. Martín-Carrón, A. de Andrés, M. T. Casais, M. J. Martínez-Lope and J. A. Alonso, *Phys. Rev. B: Condens. Matter Mater. Phys.*, 2002, **66**, 174308.
- 48 W. Kong, A. Rahimi-Iman, G. Bi, X. Dai and H. Wu, *J. Phys. Chem. C*, 2016, **120**, 7606–7611.
- 49 Q. Chen, H. Liu, H.-S. Kim, Y. Liu, M. Yang, N. Yue, G. Ren, K. Zhu, S. F. Liu, N.-G. Park, and Y. Zhang, [arXiv.org: arXiv.org >cond-mat > arXiv:1604.03760](https://arxiv.org/abs/1604.03760), submitted 10 April 2016.
- 50 M. G. Albrecht and M. Green, *J. Phys. Chem. Solids*, 1977, **38**, 297–306.
- 51 F. Verwey, *J. Phys. Chem. Solids*, 1970, **31**, 163–168.
- 52 S. Meloni, T. Moehl, W. Tress, M. Franckevicius, M. Saliba, Y. H. Lee, P. Gao, M. K. Nazeeruddin, S. M. Zakeeruddin, U. Rothlisberger and M. Graetzel, *Nat. Commun.*, 2016, **7**, 10334.
- 53 A. Walsh, D. O. Scanlon, S. Chen, X. G. Gong and S.-H. Wei, *Energy Environ. Sci.*, 2015, **8**, 995–1004.
- 54 G. Xing, N. Mathews, S. Sun, S. S. Lim, Y. M. Lam, M. Grätzel, S. Mhaisalkar and T. C. Sum, *Science*, 2013, **342**, 344–347.

- 55 R. Gottesman, L. Gouda, B. S. Kalanoor, E. Haltzi, S. Tirosh, E. Rosh-Hodesh, Y. Tischler, A. Zaban, C. Quarti, E. Mosconi and F. De Angelis, *J. Phys. Chem. Lett.*, 2015, **6**, 2332.
- 56 H.-H. Fang, F. Wang, S. Adjokatse, N. Zhao and M. A. Loi, *Adv. Funct. Mater.*, 2016, **26**, 4653.
- 57 J. F. Galisteo-López, M. Anaya, M. E. Calvo and H. Míguez, *J. Phys. Chem. Lett.*, 2015, **6**(12), 2200–2205.
- 58 J. H. Rho, J. Y. Kim, C. Lee, K. J. Lee and E. Choi, *J. Lumin.*, 2011, **131**, 1813–1816.
- 59 S. D. Stranks, V. M. Burlakov, T. Leijtens, J. M. Ball, A. Goriely and H. J. Snaith, *Phys. Rev. Appl.*, 2014, **2**, 034007.
- 60 W.-J. Yin, T. Shi and Y. Yan, *Adv. Mater.*, 2014, **26**, 4653–4658.
- 61 W.-J. Yin, T. Shi and Y. Yan, *Appl. Phys. Lett.*, 2014, **104**, 063903.
- 62 Y. Tian, M. Peter, E. Unger, M. Abdellah, K. Zheng, T. Pullerits, A. Yartsev, V. Sundström and I. G. Scheblykin, *Phys. Chem. Chem. Phys.*, 2015, **17**, 24978–24987.
- 63 T. T. Shi, W. J. Yin and Y. F. Yan, *J. Phys. Chem. C*, 2014, **118**, 25350–25354.